



Contents lists available at ScienceDirect

# Journal of Rock Mechanics and Geotechnical Engineering

journal homepage: [www.jrmge.cn](http://www.jrmge.cn)

## Full Length Article

# Evaluation of spatial variability characteristics based on anisotropic modes of random fields

Kejing Chen<sup>a</sup>, Qinghui Jiang<sup>b,\*</sup><sup>a</sup> School of Civil Engineering and Transportation, Nanchang HangKong University, Nanchang, 330063, China<sup>b</sup> School of Civil Engineering, Wuhan University, Wuhan, 430072, China

## ARTICLE INFO

### Article history:

Received 4 September 2024

Received in revised form

1 March 2025

Accepted 17 March 2025

Available online xxx

### Keywords:

Conditional random field (CRF)

Anisotropic mode

Kriging

Bayesian method

Variogram

## ABSTRACT

This paper introduces a framework for modeling random fields, with a particular emphasis on analyzing anisotropic spatial variability. It establishes a clear connection between the correlation function and the Kriging variogram across various anisotropic modes, providing mathematical models to enhance our understanding of random fields. A new anisotropy index, called  $LS_{AI}$ , is introduced to quantify anisotropy based on the autocorrelation length and the orientation of the principal axes within the variogram. An  $LS_{AI}$  value closer to one indicates a lower degree of anisotropy. The present study examines how the degree of anisotropy varies with different autocorrelation lengths and angles between the principal axes, providing valuable insights into these relationships. To improve the accuracy of parameter probability distribution estimations, this study integrates limited field test data using a Bayesian inference approach. Additionally, the Markov chain Monte Carlo simulation method is employed to develop a conditional random field (CRF) for the deformation modulus. By incorporating data from field bearing plate tests, the posterior variance data for the deformation modulus are derived. This process facilitates the construction of a detailed and reliable CRF for the deformation modulus.

© 2025 Institute of Rock and Soil Mechanics, Chinese Academy of Sciences. Published by Elsevier B.V. This is an open access article under the CC BY-NC-ND license (<http://creativecommons.org/licenses/by-nc-nd/4.0/>).

## 1. Introduction

The variation of geotechnical parameters in soil and rock masses is influenced by several factors, including changes in external forces and fluctuations in environmental temperature (Konkol, 2023; You et al., 2024). Traditional geotechnical engineering methods often struggle to accurately determine these variations, primarily because they typically overlook the spatial variability of the parameters (Montoya-Noguera and Lopez-Caballero, 2023). To address this limitation, random field theory offers a robust approach that accounts for the spatial structural variability of geotechnical parameters (Vanmarcke, 2010; Chien et al., 2022; Pandey et al., 2022). This theory enhances the understanding of how soil and rock masses respond under different conditions. Importantly, random field theory recognizes that geotechnical parameters possess both stochastic and structural

characteristics, which exhibit self-correlation (Wang et al., 2018; Zhang et al., 2022). In other words, the values of these parameters at one location are linked to those at nearby locations (Sasanian et al., 2020; Geyer et al., 2021).

Numerous studies conducted by various scholars have highlighted the significant impact of spatial variability in geotechnical parameters, especially within soil materials. This variability plays a crucial role in critical issues such as instability (Maleki et al., 2023), foundation settlement (Bungenstab and Bicalho, 2016), and the construction of parameters (Guajardo et al., 2024). However, these studies have primarily assumed structural isotropy or transverse isotropy, which may not fully reflect the complexities encountered in real-world situations. Recent advancements have introduced various methods for analyzing the spatial variability of geotechnical parameters. For instance, Guan et al. (2024) developed a machine learning technique that leverages data-driven insights to characterize this variability. Ching et al. (2023) compared two probabilistic models, namely sparse Bayesian learning and Gaussian process regression, in simulating the spatial variability of geotechnical parameters. Additionally, Zhang et al. (2025) demonstrated the Bayesian conditional co-simulation method to

\* Corresponding author.

E-mail address: [jqh1972@whu.edu.cn](mailto:jqh1972@whu.edu.cn) (Q. Jiang).

Peer review under responsibility of Institute of Rock and Soil Mechanics, Chinese Academy of Sciences.

create a robust analytical model, illustrating its application using multi-source sparse data.

Chwala et al. (2023) provided an overview of the evolution of engineering risk assessment in geotechnical engineering, particularly concerning soil, from 1960 to the present. Additionally, they outlined generalized modeling of spatial variability with random field theory and dealt with the constraints of insufficient data with a Bayesian approach. Due to the interplay of tectonic and geologic effects, surrounding rock stress, human engineering activities, and rock mass properties, rock mass parameters often have a certain degree of uncertainty (Pandit and Sivakumar Babu, 2021). To effectively express the uncertainty of geotechnical parameters, probability distributions based on statistical characteristics are increasingly recognized as an effective approach (Mazraehli and Zare, 2020). Our research, therefore, aims to focus on the spatial variability and uncertainty of parameters in rocky slopes.

Intact rocks generally exhibit poor mechanical properties due to discontinuities, which significantly influence the mechanical properties of the rock mass (Jeffery et al., 2021; Tian, 2023). These discontinuities also impact the spatial variability of rock mass parameters (Gravanis et al., 2014; Liu and Leung, 2018). Therefore, it is necessary to explore methods for characterizing the spatial variability of these parameters in rock formations with different fracture directions. Meanwhile, to account for the anisotropy of the rock mass spatial correlation function, an index is required to evaluate anisotropy (Jiang et al., 2017; Chen and Jiang, 2023).

To address the aforementioned issues, the present study proposes a framework for analyzing the spatial variability of fractured rock masses. It achieves the construction of a random field by deriving the covariance of different random field models. Additionally, a conditional random field (CRF) is established by combining variograms with the Kriging method. The anisotropy index  $LS_{AI}$  is formulated using the autocorrelation lengths ( $\delta_h$  and  $\delta_v$ ) along with the angles of the principal axes. This study explores how variations in autocorrelation lengths and the orientations of the principal axes impact the spatial variability of the modeled random field. Additionally, the CRF model is constructed by using the field data for enhanced accuracy.

## 2. Method

Rock bodies contain discontinuities such as jointed fractures and faults. The properties influenced by these discontinuities are unevenly distributed and can vary significantly in different locations (Riquelme et al., 2015). These properties may include the geometries of fractures as well as strength, deformation, and permeability parameters associated with fracture development (Bonneau et al., 2016; Marrett et al., 2018). This spatial variability arises from sedimentation, leading to the formation and deformation of shear zones or structural bodies (Han et al., 2023). Natural or engineered structural geotechnical bodies may exhibit spatial variations due to discontinuities or weaker interbedded zones. To illustrate the implementation of the methodology proposed in this study, a flowchart is provided in Fig. 1. The following steps outline the process:

- (1) Step 1: Choose the appropriate variogram to create a mathematical model for Kriging interpolation.
- (2) Step 2: Develop models that capture the diverse anisotropies in the fractured rock masses.
- (3) Step 3: Employ the Bayesian method to integrate the limited field test data, yielding a posterior distribution of geotechnical parameters.

- (4) Step 4: Combine the insights from Steps 1 and 2 to create variograms tailored to different anisotropic scenarios, optimizing model performance.
- (5) Step 5: Construct the appropriate parameter random field model by integrating the results from Steps 3 and 4.
- (6) Step 6: Based on the findings from Step 4, develop the corresponding function  $\Gamma$  for different anisotropic conditions and introduce an index  $LS_{AI}$  to evaluate the degree of anisotropy.

### 2.1. Kriging method

The Kriging method is a mathematical technique for determining interrelationships between parameters within a specific region (Krige, 1951). This interpolation method utilizes input parameters, spatial locations, and weighting coefficients to generate spatial prediction models (Rasel et al., 2023). This capability has led to a wide range of applications for estimating various natural resource parameters. By implementing Kriging, one can not only uncover the statistical characteristics of rock parameters but also capture their spatial variation. This makes it an effective tool for parametric probabilistic modeling in practical engineering scenarios. Moreover, the method's flexibility is enhanced by the availability of various variational function models, which are customized to accommodate different data distributions and autocorrelation patterns, thereby ensuring optimal outcomes across a range of applications. To achieve the spatial characterization of the fractured rock mass, this section employs the Gaussian model as the variogram used for the subsequent analysis. The formula for the variogram of the Kriging method is as follows:

$$\gamma(h) = n \left\{ 1 - \exp \left[ - \left( \frac{h}{l} \right)^2 \right] \right\} + n_0 \quad (1)$$

where  $n_0$  represents the nugget value, which is taken as 0 when not specified later;  $n = \sigma^2$ , in which  $\sigma$  denotes the standard deviation of the parameter;  $n + n_0$  represents the sill value;  $h$  represents the lag distance; and  $l$  represents the autocorrelation length.  $\gamma(h)$  is defined on the range  $[n_0, n + n_0]$ . The corresponding Gaussian-type covariance function and correlation coefficient are:

$$C(h) = n \exp \left[ - \left( \frac{h}{l} \right)^2 \right] \quad (2)$$

$$\xi(h) = \exp \left[ - \left( \frac{h}{l} \right)^2 \right] \quad (3)$$

### 2.2. Random field mode

To investigate the spatial variation characteristics of geotechnical body parameters, Zhu and Zhang (2013) generalized five common anisotropy modes of natural fractured rock masses (Fig. 2), which relate the fracture development direction to the two main directions of the strongest and weakest autocorrelation. As illustrated in Table 1, the red lines indicate the directions associated with autocorrelation lengths for different modes. The anisotropy of deformation and permeability in fractured rock masses is closely related to the fracture direction. Therefore, this section constructs the variogram based on different fracture directions and examines the anisotropy of the corresponding parameters of the random field.

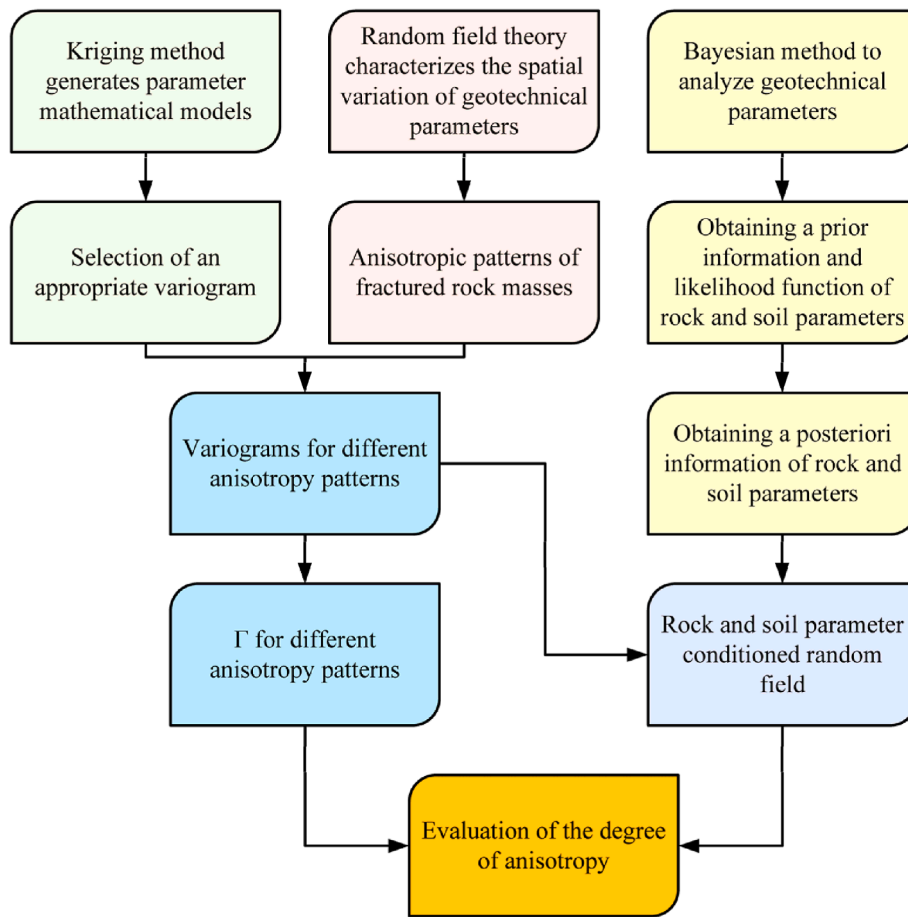


**Fig. 1.** Flowchart for the proposed method.

Zhu and Zhang (2013) developed functional expressions to describe the relative distances between two points in arbitrary space, taking into account different anisotropic modes through coordinate rotation and correction. The correlation scales for these modes are represented in Table 1, where the red solid arrows indicate the direction of the spatially varying principal axes and the green dashed arrows represent the direction of the correlation scales. The variables are defined as follows:  $\theta$  is the direction angle;  $\varphi$  is the rotation angle (modes c and e);  $\omega$  is the acute angle between the two principal axes when they are not perpendicular (modes d and e);  $\Delta x$  and  $\Delta y$  represent the Euclidean distances between the two observation points along the horizontal and vertical directions, respectively; and  $\delta_\theta$  denotes the correlation scale. Combining the direction angle with the definitions of  $\Delta x$  and  $\Delta y$  gives the corresponding transformation relation:  $\Delta y/\Delta x = \tan\theta$ .

### 2.3. Bayesian method

The Kriging method, as described in Eq. (1), is effective for creating a parametric CRF, relying on the determination of the variance value, known as the  $n$  value. However, due to challenging geological conditions and budget constraints, project teams often face the issue of limited monitoring and testing data. In such cases, the application of Bayesian methods can prove advantageous. It leverages the scant information available to infer the probability distribution of parameters and estimate their statistical characteristics effectively (Wang and Cao, 2013; Ering and Babu, 2016; Papaioannou and Straub, 2017; Liu et al., 2022). By overcoming

the limitation of only obtaining limited information (including both field and laboratory test results) about the geotechnical parameters, the Bayesian approach has emerged as a reliable choice in the realm of geotechnical engineering. At its core, the Bayesian method consists of three key components: prior information, likelihood function, and posterior information. The calculation of the posterior probability density function for the geological parameter  $\alpha$  is articulated as follows:

$$f_{X|\alpha}(\mathbf{x}) \propto L(\mathbf{x})f_\alpha(\mathbf{x}) \quad (4)$$

where  $f_{X|\alpha}(\mathbf{x})$ ,  $L(\mathbf{x}) = f_{X|\alpha}(\mathbf{x})$  and  $f_\alpha(\mathbf{x})$  represent the posterior, likelihood, and a priori probability density functions of the geologic parameter  $\alpha$ , respectively.

A priori information is essential for understanding the distribution characteristics of geotechnical parameters, which are initially identified through prior investigations, field tests, or engineering experience. When a significant amount of test data is available (indicating strong a priori information), the data can be effectively utilized to accurately determine the distribution of geotechnical parameters. In situations where the prior information is limited (weak a priori information), the implementation of a non-informative prior (commonly accepted probability distributions in geotechnical engineering) offers a way to express the inherent uncertainty surrounding these parameters.

The likelihood function serves as a probability tool for quantifying the uncertainty of geotechnical parameters. In the field of geotechnical engineering, measurement errors are an inevitable occurrence. The application of the likelihood function facilitates

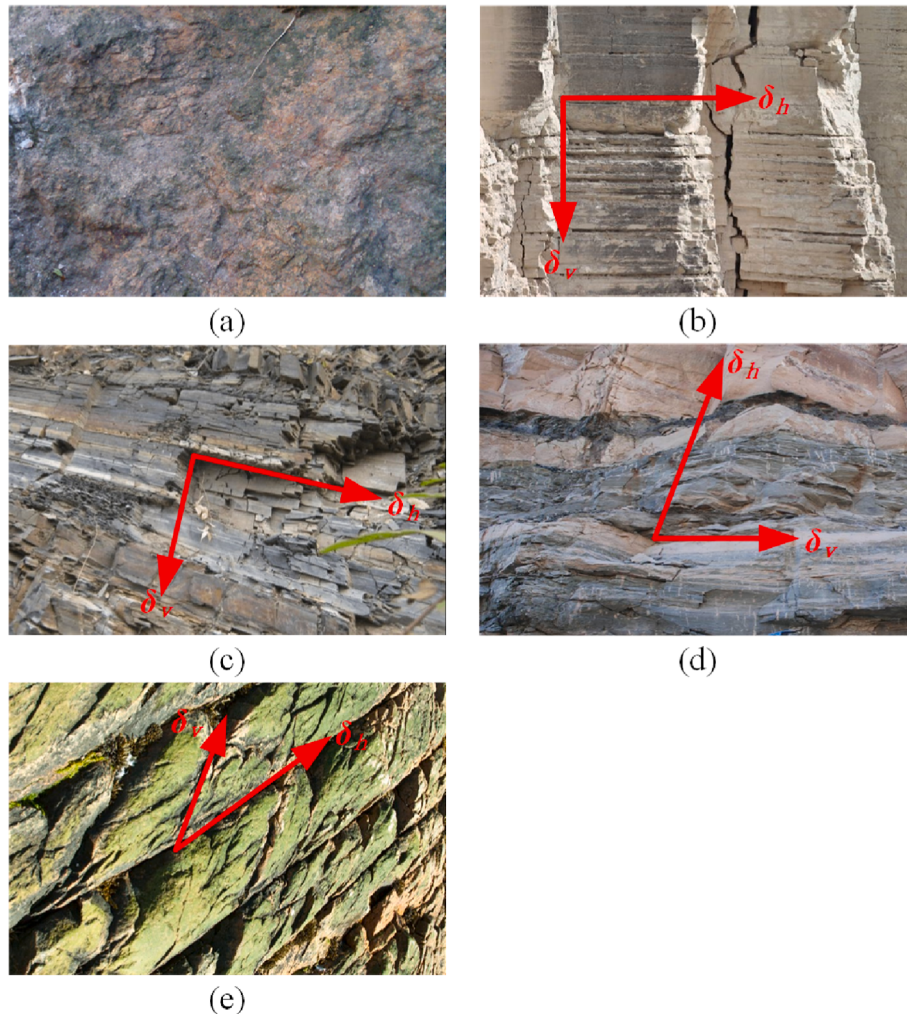


**Fig. 2.** Schematic representation of the rock profile in each mode: (a) Structural isotropy; (b) Structural transverse anisotropy; (c) Anisotropy (presence of rotation angle); (d) General anisotropy; and (e) General anisotropy (presence of rotation angle).

the effective articulation of the uncertainty stemming from these errors.

### 3. Random field anisotropy

The implementation of spatial random field generation and the Kriging method depends on two functions: the covariance function and the variogram. These functions establish essential parameters such as autocorrelation length, dimension, variance, and the distance between two points. The covariance function plays a critical role in generating spatial random fields, especially when monitoring the values of target parameters. Additionally, CRFs can be constructed by integrating the Kriging method with random field generation techniques. In this section, the paper will explore the covariance function and variogram under different anisotropy modes, derive the anisotropy index, and analyze how changes in relevant parameters affect it.

#### 3.1. Variogram for different random field modes

The autocorrelation function is a key tool that describes the variation of geotechnical parameters and illustrates the correlation between two spatial points. As mentioned in Section 2.1, the

autocorrelation function used in this section is of the Gaussian type. Eq. (5) presents the expression for the two-dimensional (2D) autocorrelation coefficient:

$$\rho(\tau_x, \tau_y) = \exp \left[ - \left( \frac{\tau_x^2}{\delta_h^2} + \frac{\tau_y^2}{\delta_v^2} \right) \right] \quad (5)$$

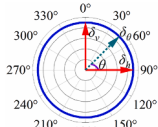
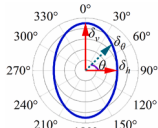
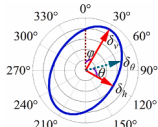
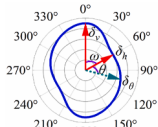
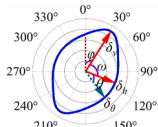
where  $\tau_x$  represents the distance between two points along one principal axis;  $\tau_y$  represents the distance between two points along the other principal axis; and  $\delta_h$  and  $\delta_v$  denote the autocorrelation lengths in the direction of the two principal axes, respectively.

Subsequently, the covariance function can be obtained under different random field modes by substituting Eq. (5) into Eq. (2). The construction of a random field involves using this covariance function, which is integrated with the stochastic process in Fourier space. This approach has the advantage of generating standard spatial random fields while ensuring the statistical properties of the parameters involved. Then, the variograms for different random field modes can be obtained, and the parameter CRFs can be derived by combining the field measurement data.

In this case, substituting Eq. (5) into Eq. (1) can yield the following equation:

**Table 1**

Correlation scales for each mode.

Mode	Correlation scale	Formulae
a		$\tau_x = \Delta x$ $\tau_y = \Delta y$ $\delta_\theta = \delta_h = \delta_v$
b		$\tau_x = \Delta x$ $\tau_y = \Delta y$ $\delta_\theta = \sqrt{\frac{\delta_h^2 \delta_v^2 (1 + \tan^2 \theta)}{\delta_h^2 \tan^2 \theta + \delta_v^2}}$
c		$\tau_x = \Delta x \cos \varphi + \Delta y \sin \varphi$ $\tau_y = -\Delta x \sin \varphi + \Delta y \cos \varphi$ $\delta_\theta = \sqrt{\frac{\delta_h^2 \delta_v^2 (1 + \tan^2 \theta)}{\delta_h^2 (-\sin \varphi + \cos \varphi \tan \theta)^2 + \delta_v^2 (\cos \varphi + \sin \varphi \tan \theta)^2}}$
d		$\tau_x = \Delta x + \Delta y \cot \omega$ $\tau_y = \Delta y$ $\delta_\theta = \sqrt{\frac{\delta_h^2 \delta_v^2 (1 + \tan \theta \cot \omega)^2 + \delta_h^2 \delta_v^2 \tan^2 \theta}{\delta_h^2 \tan^2 \theta + \delta_v^2 (1 + \tan \theta \cot \omega)^2}}$
e		$\tau_x = (\Delta x + \Delta y \cot \omega) \cos \varphi + \Delta y \sin \varphi$ $\tau_y = -(\Delta x + \Delta y \cot \omega) \sin \varphi + \Delta y \cos \varphi$ $\delta_\theta = \sqrt{\frac{\delta_h^2 \delta_v^2 (1 + \tan \theta \cot \omega)^2 + \delta_h^2 \delta_v^2 \tan^2 \theta}{\delta_h^2 [-(1 + \tan \theta \cot \omega) \sin \varphi + \tan \theta \cos \varphi]^2 + \delta_v^2 [(1 + \tan \theta \cot \omega) \cos \varphi + \tan \theta \sin \varphi]^2}}$

$$\gamma(h) = n \left\{ 1 - \exp \left[ - \left( \frac{\tau_x^2}{\delta_h^2} + \frac{\tau_y^2}{\delta_v^2} \right) \right] \right\} + n_0 \quad (6)$$

The Kriging Gaussian variograms for different random field modes can be obtained by substituting the computational expressions of  $\tau_x$  and  $\tau_y$  in Table 1 into Eq. (6). After determining the specific variograms, the optimal weighting coefficients can be combined with the measured field data to perform Kriging interpolation across the entire region, resulting in a parameter CRF. Table 2 presents a list of the Gaussian variogram based on the Kriging method in different modes. These formulas can realize the corresponding parameter random field generation.

### 3.2. Anisotropy for different random field modes

As illustrated in Table 2, the variability function is typically defined in terms of  $\Delta x$ ,  $\Delta y$ ,  $\delta_h$ , and  $\delta_v$ . The general geotechnical parameters are categorized as either structural isotropic or transverse anisotropic modes. However, numerous geotechnical parameters exhibit anisotropy, indicating that they possess varying correlation distances depending on the direction. For example, the anisotropy observed in rock deformation and permeability properties is often attributed to the fracture distribution.

This section aims to investigate random field models across different modes, linking the anisotropy in fracture distribution to

**Table 2**  
Variograms for each mode.

Mode	Formulae
a	$\gamma(h) = n \left\{ 1 - \exp \left[ - \left( \frac{\Delta x^2}{\delta_h^2} + \frac{\Delta y^2}{\delta_v^2} \right) \right] \right\} + n_0$
b	$\gamma(h) = n \left\{ 1 - \exp \left[ - \left( \frac{\Delta x^2}{\delta_h^2} + \frac{\Delta y^2}{\delta_v^2} \right) \right] \right\} + n_0$
c	$\gamma(h) = n \left\{ 1 - \exp \left[ - \frac{(\Delta x \cos \varphi + \Delta y \sin \varphi)^2}{\delta_h^2} - \frac{(-\Delta x \sin \varphi + \Delta y \cos \varphi)^2}{\delta_v^2} \right] \right\} + n_0$
d	$\gamma(h) = n \left\{ 1 - \exp \left[ - \frac{(\Delta x + \Delta y \cot \omega)^2}{\delta_h^2} - \frac{(\Delta y)^2}{\delta_v^2} \right] \right\} + n_0$
e	$\gamma(h) = n \left\{ 1 - \exp \left\{ - \frac{[(\Delta x + \Delta y \cot \omega) \cos \varphi + \Delta y \sin \varphi]^2}{\delta_h^2} - \frac{[-(\Delta x + \Delta y \cot \omega) \sin \varphi + \Delta y \cos \varphi]^2}{\delta_v^2} \right\} \right\} + n_0$

the anisotropy in random fields, with consideration given to correlation scales. If two groups of fracture distributions lead to permeability exhibiting structural transverse anisotropy, then the associated anisotropy of the permeability random field should also be expressed as structural transverse anisotropy. An expression for evaluating the anisotropy based on the autocorrelation coefficient is presented as follows:

$$\Gamma = \sqrt{\frac{\tau_x^2}{\delta_h^2} + \frac{\tau_y^2}{\delta_v^2}} = \frac{\tau_x}{\delta_h} \sqrt{1 + \frac{\tau_y^2}{\tau_x^2} \left( \frac{\delta_h}{\delta_v} \right)^2} \quad (7)$$

where  $\delta_h/\delta_v$  is referred to as the ratio of autocorrelation lengths to evaluate the degree of anisotropy.

From the figures in Table 1,  $\Delta y/\Delta x = \tan\theta$ , which can be substituted into Eq. (7) to derive the expression of  $\Gamma$  under different anisotropic modes (see Table 3). When  $\delta_h/\delta_v$  changes, the degree of anisotropy also changes, and this degree remains constant during rotation in any mode. When the principal axes are not perpendicular, this degree is adjusted using a dimensionless quantity ( $\cot\omega$ ), which relates to the angle between the principal axes. The degree of anisotropy index is shown as follows:

$$LS_{AI} = \begin{cases} (1 + \cot\omega) \frac{\max(\delta_h, \delta_v)}{\min(\delta_h, \delta_v)} & (\delta_h \neq \delta_v) \\ 1 & (\delta_h = \delta_v) \end{cases} \quad (8)$$

where  $LS_{AI} = \delta_h/\delta_v$  when the principal axes are vertical ( $\omega = 90^\circ$ ), assuming  $\delta_h > \delta_v$ . It is worth mentioning that when  $\delta_h = \delta_v$ ,  $\delta_\theta = \delta_h = \delta_v$ , indicating structural isotropy. At this time,  $\omega$  will equal  $90^\circ$ , then  $LS_{AI} = 1$ .

The degree of anisotropy index  $LS_{AI}$  has several important properties:

- (1) When the principal axes are orthogonal (horizontal and vertical) and  $\delta_h = \delta_v$ ,  $LS_{AI} = 1$ . This indicates that the random field exhibits structural isotropy. If the principal axes are orthogonal and  $\delta_h \neq \delta_v$ , the random field shows structural transverse anisotropy.
- (2) In practical engineering, the orthogonal principal axes are not always strictly horizontal and vertical. A certain rotation angle may need to be considered. For instance, the transformation between structural transverse anisotropy and the anisotropy (presence of rotational angle) can be achieved through coordinate rotation. In two dimensions, this rotation is represented by a single angle ( $\varphi$  in Table 1). When the principal axes are orthogonal (rotational angle exists), and  $\delta_h \neq \delta_v$ , the random field demonstrates anisotropy due to this rotational angle.

**Table 3**  
 $\Gamma$  for each mode.

Mode	Formulae
a	$\Gamma = \frac{\Delta x}{\delta_h} \sqrt{1 + \tan^2 \theta \left( \frac{\delta_h}{\delta_v} \right)^2}$
b	$\Gamma = \frac{\Delta x}{\delta_h} \sqrt{1 + \tan^2 \theta \left( \frac{\delta_h}{\delta_v} \right)^2}$
c	$\Gamma = \frac{-\Delta x \sin \varphi + \Delta y \cos \varphi}{\delta_h} \sqrt{1 + \tan^2(\theta - \varphi) \left( \frac{\delta_h}{\delta_v} \right)^2}$
d	$\Gamma = \frac{\Delta x + \Delta y \cot \omega}{\delta_h} \sqrt{1 + \left( \frac{1}{\cot \theta + \cot \omega} \right)^2 \left( \frac{\delta_h}{\delta_v} \right)^2}$
e	$\Gamma = \frac{(\Delta x + \Delta y \cot \omega) \cos \varphi + \Delta y \sin \varphi}{\delta_h} \sqrt{1 + \left[ \frac{-(\cot \theta + \cot \omega) \tan \varphi + 1}{\cot \theta + \cot \omega + \tan \varphi} \right]^2 \left( \frac{\delta_h}{\delta_v} \right)^2}$

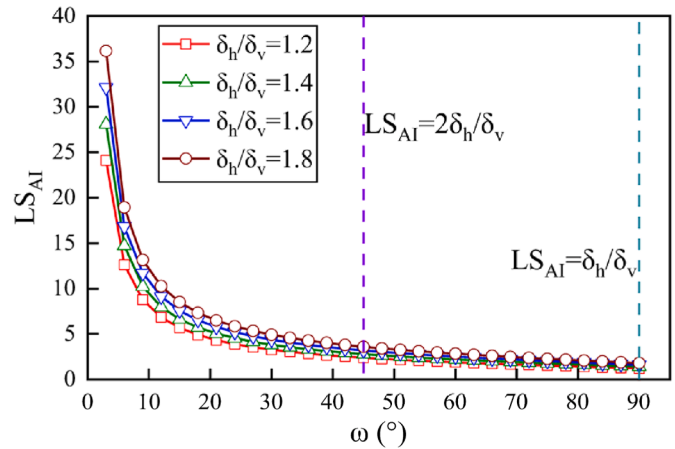


**Fig. 3.** Relationship between autocorrelation length,  $\omega$  and  $LS_{AI}$ .

- (3) When  $LS_{AI}$  approaches 1, the degree of anisotropy decreases.
- (4) When the principal axes are not orthogonal (rotation angle exists), and  $\delta_h \neq \delta_v$ , the angle between the principal axes can be adjusted to evaluate the degree of anisotropy. The closer the two principal axes, the smaller the acute angle between them, the greater the degree of anisotropy, and vice versa.

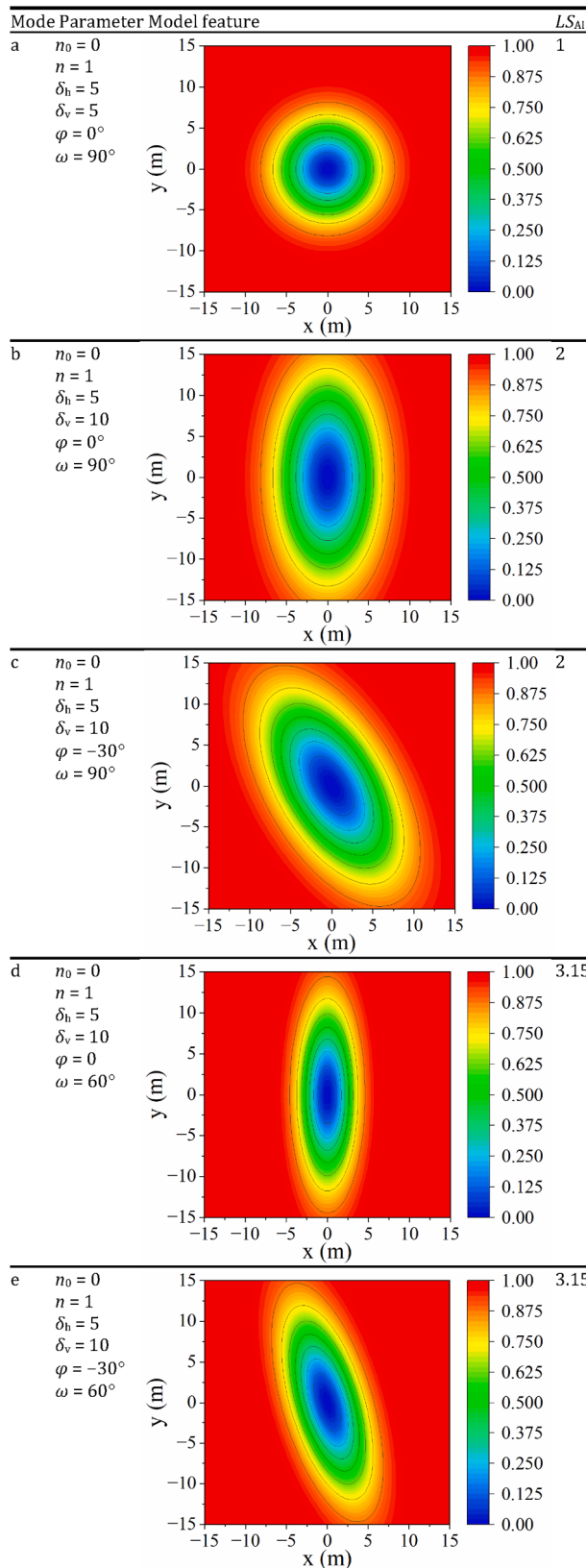
As shown in Fig. 3, the dot-line plots of the anisotropy index  $LS_{AI}$  under different autocorrelation length conditions are displayed as a function of the angle  $\omega$  formed by the acute angle between the principal axes. The values of  $\omega$  in the figure range from  $3^\circ$  to  $90^\circ$ , with an interval of  $3^\circ$ . Fig. 3 indicates that when  $\omega$  is small, the changes in  $LS_{AI}$  are pronounced. As  $\omega$  increases, the rate of change in  $LS_{AI}$  gradually slows down. Under the same  $\omega$  condition, a larger  $\delta_h/\delta_v$  indicates a higher degree of anisotropy.

The spatial variability functions and parameters utilized across different modes are detailed in Table 4. To enhance the intuitiveness of the model, the extent of the study area is  $-15-15$  m ( $-3\delta_h$  to  $3\delta_h$ ) in both the  $x$  and  $y$  directions, with each direction divided into 50 intervals of 0.6 m. This results in a total of 2500 plotted data points. The coordinate origin is established at the center of the first grid, ensuring that the variogram model maintains symmetry about this origin.

The  $LS_{AI}$  values for the different modes are also presented in Table 4. The  $LS_{AI}$  values for all modes, with the exception of the structural isotropy mode, exceed 1. The  $LS_{AI}$  values for modes b and c are both 2, while modes d and e demonstrate  $LS_{AI}$  values of 3.15, indicating that the occurrence of rotations under identical conditions has no impact on the degree of anisotropy of the random

**Table 4**

Structure of the spatial variogram in each mode.

field, i.e. the  $LS_{AI}$  value is independent of the coordinate axis.

The random field models and their parameters for different modes are summarized in Table 5. The study area ranges from 0 m to 100 m along both the  $x$  and  $y$  axes, which are divided into 100 segments with 1 m intervals. Ten thousand data points are plotted for the model in the figure. When the angle between the principal axes and the autocorrelation length remains consistent, the distribution pattern of the generated random field models in each mode aligns with the structure of the spatial variability function, indicating that the proposed method is reliable for developing parametric random field models.

### 3.3. Parameter sensitivity analysis

Firstly, a homogeneous rock mass is used as the study object. Mode a in Table 5 is used as an example ( $\delta_h = \delta_v$ ) for the analysis. The grid configurations align with those outlined in Table 5. This study analyzes different correlation lengths to effectively characterize how they affect the spatial variability of rock mechanical parameters (Al-Bittar and Soubra, 2017). Random field models are developed based on different main correlation lengths, specifically detailed in Table 6 ( $\delta_h = 5, 10$ , and  $15$ ). When  $\delta_h \rightarrow \infty$ , the parameters converge to a single random variable with the same parameter values across the entire region. To simplify implementation, this "infinite" condition is approximated with  $\delta_h$  set to 1000. As  $\delta_h$  increases, the fluctuations in the parameter within the random field model diminish. Therefore, utilizing the random field method to assess the spatial variability of the parameters is more reasonable than relying on a single random variable approach.

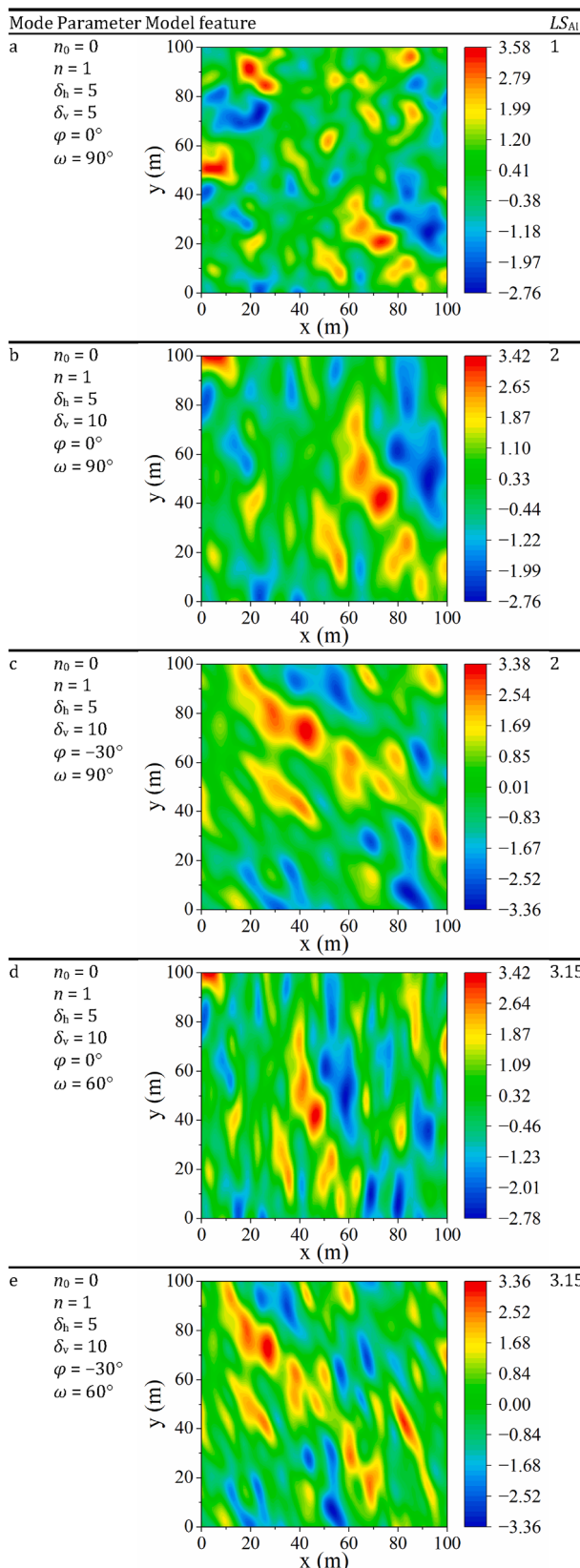
The parametric random field modeling method can construct random field models with different rotation angles, autocorrelation lengths, and angles between principal axis directions. The rock mass characterized in Fig. 2e serves as the study object. As illustrated in Fig. 4, mode e in Table 5 is an illustrative example. The main correlation length and the rotation angle  $\varphi$  are critical parameters in this mode. Consequently, the effects of different anisotropy values and main correlation directions on the random field model are investigated by comparing different main correlation lengths and  $\varphi$ .

The model has dimensions of 100 m  $\times$  100 m, with a grid size of 1 m  $\times$  1 m. The values for  $\varphi$  are set at  $15^\circ, 45^\circ$ , and  $75^\circ$ , while  $\delta_v$  is set at 1, 2, and 3, respectively. The  $LS_{AI}$  values listed in Table 6 are all equal to 1. For comparative analysis, the  $LS_{AI}$  values in Fig. 4 are 2, 4, and 6, respectively, allowing the corresponding values of  $\delta_h$  to be determined according to Eq. (8).

As shown in Fig. 4, for a given rotation angle  $\varphi$ , the correlation of the parameters along the direction of  $\varphi$  increases with higher  $LS_{AI}$  values, while the correlation of the parameters perpendicular to the direction of  $\varphi$  remains unchanged. The parameters in the two directions exhibit different levels of correlation, demonstrating the anisotropy characteristics of the space. This characteristic becomes increasingly pronounced as the  $LS_{AI}$  value increases. The model effectively reflects the impact of different autocorrelation lengths, and the effects of changing  $\varphi$  values on the model are also appreciable. The proposed method successfully establishes a random field model that meets the requirements.

When simulating the deformation parameters of rocky slopes using random fields, the geological model often consists of a combination of different rock layers and geological structure surfaces. This variation arises from the different degrees of fragmentation among varying rock classes and the corresponding degree of rock fracture development. To accurately reflect the actual situation, it is important to conduct a segmented analysis of the study area, ensuring coherence with adjacent areas. Additionally, as the size of different areas may vary, the mesh size

**Table 5**  
Random field model in each mode.



utilized for each area may differ accordingly. Therefore, it is imperative to maintain consistent field generation across these varying grid sizes. The proposed modeling method can accomplish the related requirements.

As illustrated in Fig. 5, the model is analyzed using the parameters aligned with those in Fig. 4f, i.e.  $\delta_h = 12$ ,  $\delta_v = 2$ , and  $\varphi = 45^\circ$ . The entire model extends from 0 m to 150 m along the  $x$ -axis and from 0 m to 100 m along the  $y$ -axis. The model is divided into two regions: the left region ( $x = 0$ –100 m,  $y = 0$ –100 m) has a grid spacing of 1 m  $\times$  1 m, while the right region ( $x = 100$ –150 m,  $y = 25$ –75 m) features a grid spacing of 0.5 m  $\times$  0.5 m. The results in Fig. 5 indicate that the overall model and the model within each subregion exhibit the same distribution pattern and degree of anisotropy. Additionally, the continuity of parameters is maintained in the connecting part between the left and right subregions.

The left region in Fig. 5 can be further subdivided into several small sub-areas. The parameters within adjacent regions can be kept consistent, allowing for new random field realizations within these small regions while maintaining parameter continuity. This enables the modifications to the random field in one small region without affecting the others. Consequently, this approach enables the extraction and exploration of essential parts during the study of the actual project, enhancing the flexibility of modeling and analysis.

#### 4. Characteristics of spatial variation of deformation modulus anisotropy

The deformation of the rock mass within the dam area is influenced by several factors, including tectonics, degree of weathering, and degree of fracture development. These factors also affect the spatial distribution pattern, leading to significant differences in the deformation modulus across different directions. In practical engineering, it is essential to study and understand the anisotropy of deformation for effective slope design and optimization. For anisotropic rock mass, it is necessary to consider and characterize the stress-strain relationship in multiple directions and its effects during the construction process.

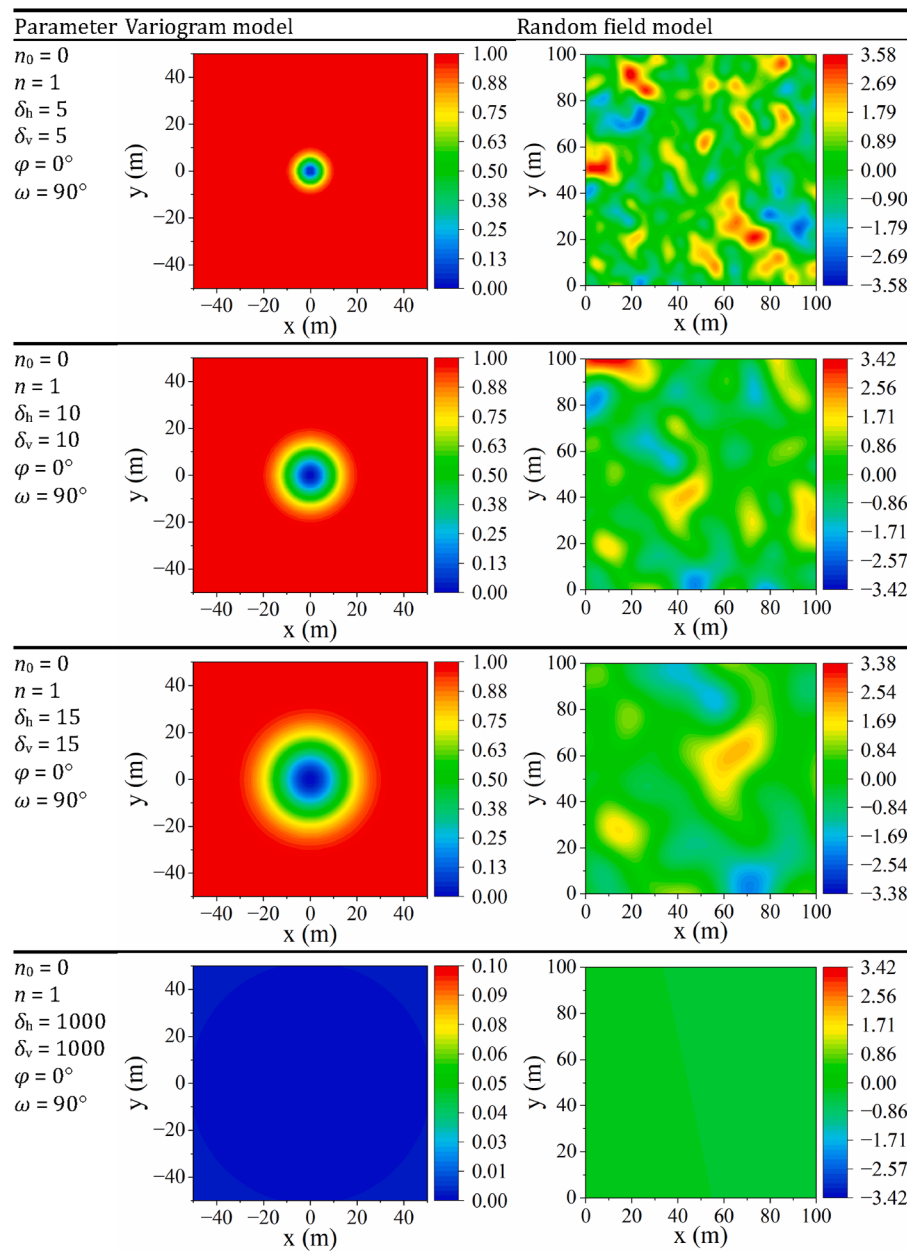
##### 4.1. Analysis of field deformation modulus

A total of 60 rock deformation test monitoring points have been established at the Jinping I Hydropower Station in China. These points were arranged based on the site's engineering geological characteristics, the rock mass quality class, and the development of fractures.

Fig. 6 shows the deformation modulus ( $E$ ) of the test points at different depths in the dam area. The horizontal and vertical depths represent the distances of the test points from the slope surface, respectively. As illustrated in Fig. 6, each test point is indicated by the center of a bubble, with the bubble size reflecting the relative magnitude of the measured deformation modulus at that point. Overall, the deformation modulus generally increases with depth. However, some test points located in a deeper crushed zone show relatively low deformation modulus values. The recorded values range from a minimum of 0.3 GPa to a maximum of 51.8 GPa. On average, the deformation modulus is approximately 15.3 GPa, with a standard deviation of about 13.4 GPa.

To evaluate the deformation modulus of rock mass, many researchers have proposed empirical formulas that utilize other relatively easy-to-obtain geotechnical parameters. These parameters include wave velocity ( $V_p$ ), rock mass block index ( $RBI$ ), rock mass rating ( $RMR$ ), geological strength index ( $GSI$ ), tunneling quality index ( $Q$ ), and rock quality designation ( $RQD$ ) (Alemadag

**Table 6**  
Random field models corresponding to different correlation lengths.



et al., 2016; Hua et al., 2021; Lasantha and Athapaththu, 2024).

To assess the comparative effectiveness of these parameters in evaluating the deformation modulus, scatter plots were generated to illustrate the relationship between deformation modulus and  $V_p$ ,  $RBI$ ,  $RQD$ , and  $Q$  (Fig. 7). The results indicate that the correlations for  $V_p$  or  $Q$  are more reliable than those for  $RQD$  and  $RBI$ . For further analysis, a power exponential regression model relating  $V_p$  to the deformation modulus is employed (Shen et al., 2017). The fitted curves in Fig. 7 demonstrate the relationship between  $V_p$  and deformation modulus, which can be expressed as follows:

$$E = 0.01V_p^{4.42} \quad (9)$$

The total number of  $V_p$  used to fit  $E$  was 49, with the minimum and maximum values being 2.11 km/s and 6.32 km/s, respectively.

The mean value was determined to be about 4.94 km/s, and the standard deviation was found to be approximately 0.94 km/s.

#### 4.2. Deformation modulus CRF

The premise of constructing a deformation modulus CRF is to determine the variance of the deformation modulus. In this section, a Bayesian framework is utilized to explore the distribution characteristics of the deformation modulus. A limitation encountered is the relatively small number of deformation modulus measurements available from the field. Numerous experiments have demonstrated that  $E$  values of rock masses typically follow either normal or lognormal distribution (Cui et al., 2017; Liu et al., 2022). Unlike the normal distribution, the lognormal distribution

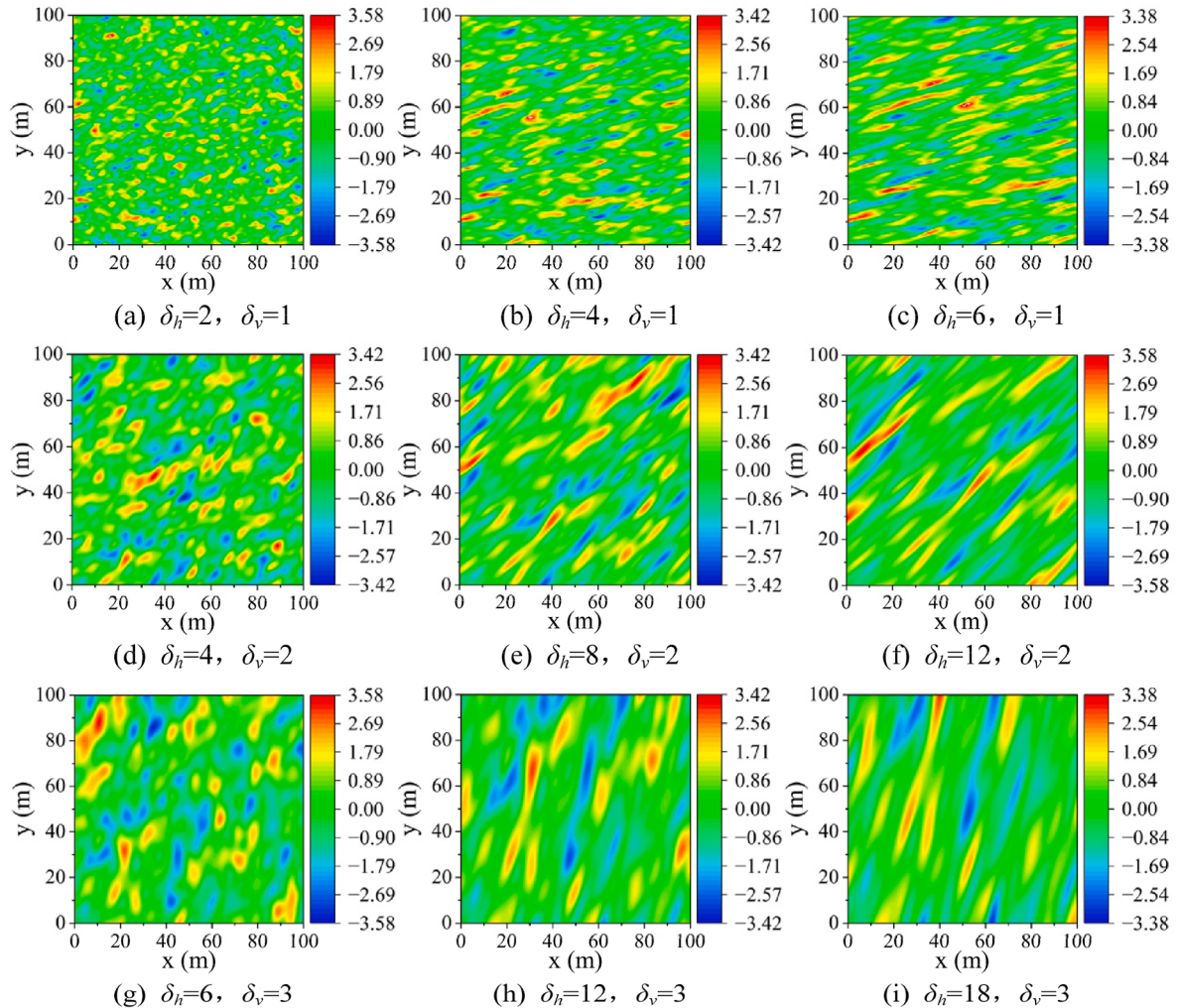


**Fig. 4.** Random field models under different autocorrelation lengths and  $\varphi$ : (a)–(c)  $\varphi = 15^\circ$ ; (d)–(f)  $\varphi = 45^\circ$ ; and (g)–(i)  $\varphi = 75^\circ$ .

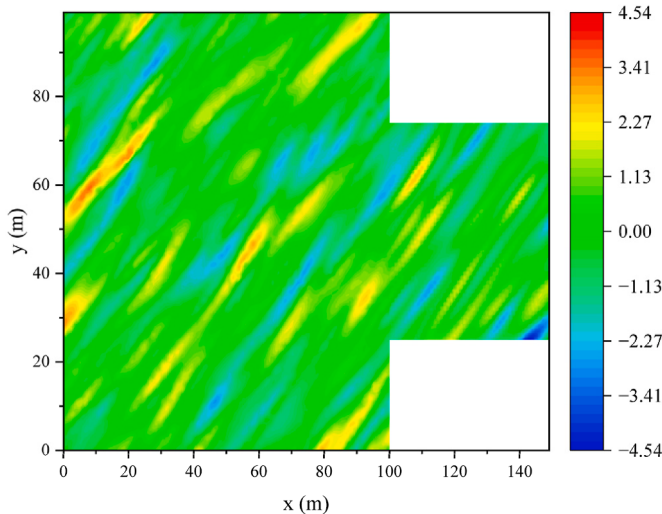


**Fig. 5.** Block area modeling diagram.

ensures that  $E$  values remain positive. Assuming that the prior probability information for the deformation modulus (bearing

plate test values) follows a lognormal distribution, the expression form of the prior probability function, along with its mean and standard deviation, can be determined. Taking the natural logarithm at both ends of Eq. (9) yields the following equation:

$$\ln V_p = 0.226 \ln E + 1.042 \quad (10)$$

where  $\ln V_p$  represents the logarithmic value of the wave velocity, which follows a normal distribution. It is clear from Fig. 7 that Eq. (10) has an associated error, thus necessitating the utilization of the symbol  $\epsilon$  to characterize the uncertainty in the model transformation. It should be pointed out that  $\epsilon$  obeys a normal distribution with a mean of 0 and a constant standard deviation. Eq. (10) can be rewritten as follows:

$$\zeta = \ln V_p = a \ln E + b + \epsilon \quad (11)$$

Since  $E$  follows a lognormal distribution, it can be deduced that  $\ln E$  follows a normal distribution. The mean and standard deviation of  $\ln E$  are defined as  $\mu_E$  and  $\sigma_E$ , respectively, while the standard deviation of  $\epsilon$  is  $\sigma_\epsilon$ . The mean and variance of  $\zeta$  are estimated from the bearing plate test data and other relevant information. Consequently,  $\zeta$  is a normally distributed random variable with a mean of  $a\mu_E + b$  and a variance of  $a^2\sigma_E^2 + \sigma_\epsilon^2$ . Additionally, for some rock wave velocity measurements collected from various field

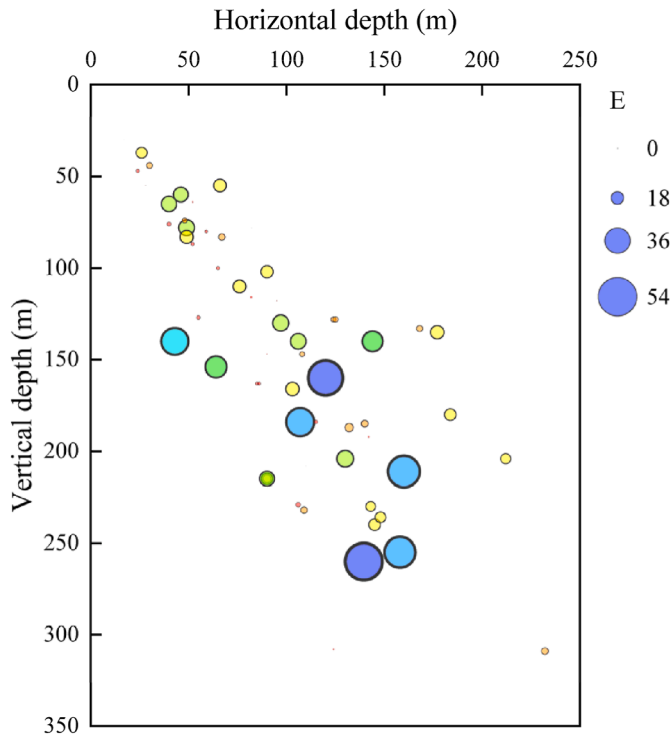


**Fig. 6.** Bubble plots of deformation modulus at different depth conditions.

locations, assuming that the measurements at these locations are independent and simplifying the logarithm of the wave velocity  $\zeta$  to several independent realizations of a Gaussian random variable, Eq. (4) can be rewritten as

$$P(\mu, \sigma | Data) \propto P(Data|\mu, \sigma)P(\mu, \sigma) \quad (12)$$

where  $P(\mu, \sigma | Data)$  denotes the  $(\mu, \sigma)$  distribution probability for the given experimental test data,  $P(Data|\mu, \sigma)$  denotes the likelihood-distributed probability of the test data, and  $Data$  represents the set of  $\zeta$ . The likelihood function concerning  $\zeta$  is expressed as

$$P(Data|\mu, \sigma) = \prod_{j=1}^n \frac{1}{\sqrt{2\pi} \sqrt{(a\sigma_E)^2 + \sigma_e^2}} \exp \left\{ -\frac{1}{2} \left[ \frac{\zeta_j - (a\mu_E + b)}{\sqrt{(a\sigma_E)^2 + \sigma_e^2}} \right]^2 \right\} \quad (13)$$

where  $n$  is the number of tests. This study adopts the method used by Liu et al. (2022) to define the standard deviation that describes uncertain  $\epsilon$  as the standard deviation of the output variable, and  $\sigma_e^2$  is taken to be 1.

In Bayesian methods for determining the posterior distributions of parameters, analytical solutions are often unattainable, necessitating numerical solutions. A prevalent methodology is the Markov chain Monte Carlo simulation, which estimates the posterior distribution by generating samples of the posterior random variable (Wang and Cao, 2013). To enhance computational efficiency, numerical calculations can be performed using 2D grid cells in the  $\mu_E$  and  $\sigma_E$  space:

$$\begin{aligned} n_\mu &= (\mu_{\max} - \mu_{\min}) / \Delta\mu_E \\ n_\sigma &= (\sigma_{\max} - \sigma_{\min}) / \Delta\sigma_E \end{aligned} \quad (14)$$

where  $\Delta\mu_E$  and  $\Delta\sigma_E$  represent the intervals for the deformation modulus within a 2D grid cell, both set at 0.1. It is assumed that  $\mu_E$  and  $\sigma_E$  follow the distributions of  $U(\mu_{\max}, \mu_{\min})$  and  $U(\sigma_{\max}, \sigma_{\min})$ , respectively, where  $U$  stands for uniform distribution. The mean of  $E$  is set to obey a uniform distribution from 10 GPa to 19 GPa, while the standard deviation follows a uniform distribution from 5 GPa to 18 GPa. The advantage of this method is that the uniform prior distribution can be predetermined using only the known ranges of the model distribution parameters, which is suitable for conditions with relatively limited prior information.

Many deformation modulus samples that match the posterior probability function can be generated. These samples facilitate the estimation of both the posterior mean and standard deviation of the deformation modulus. Fig. 8 illustrates the scatterplot of 10,000 generated posterior samples of the deformation modulus. Approximately 94.7% of these samples fall below 30 GPa, and the samples become increasingly sparse for  $E$  exceeding 30 GPa.

A frequency histogram of the posterior deformation modulus is created to examine the statistical distribution pattern of the posterior samples, as shown in Fig. 9. The analysis reveals that the posterior probability follows a lognormal distribution. For

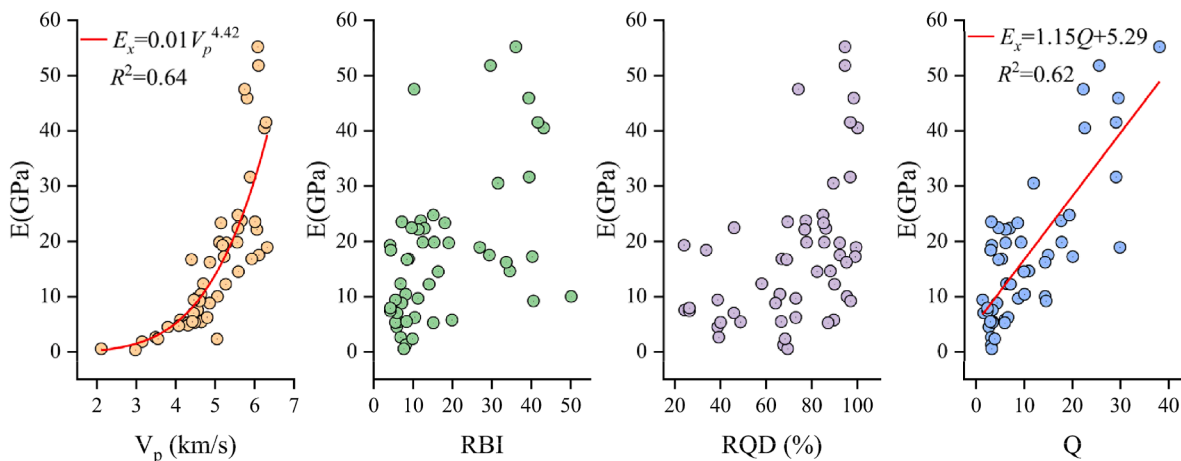


**Fig. 7.** Deformation modulus and geotechnical parameter fitting curves.

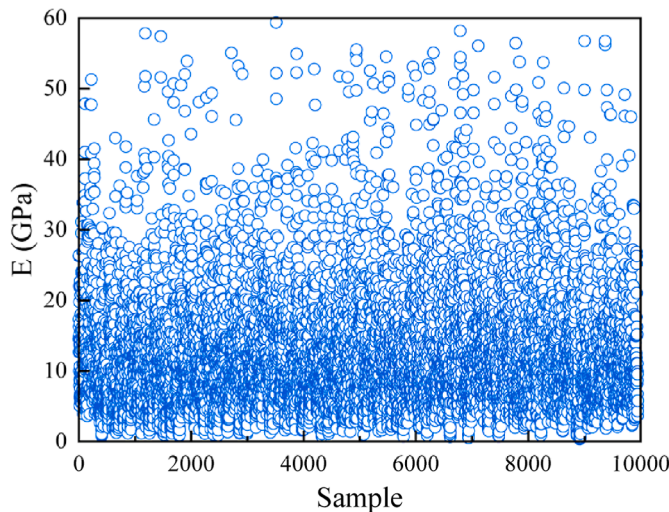


**Fig. 8.** Scatterplot of deformation modulus samples.

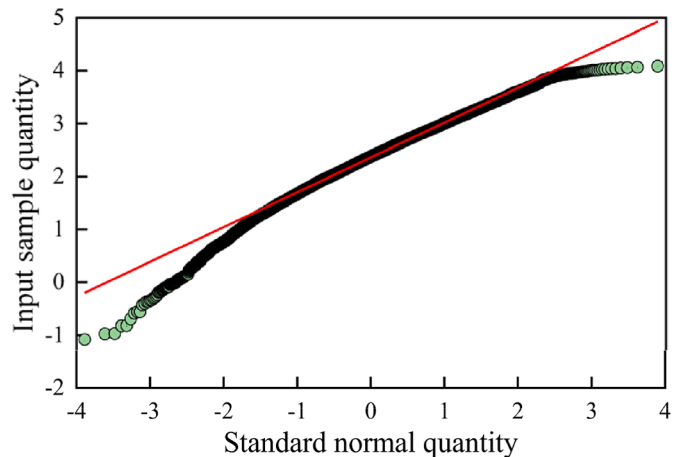


**Fig. 10.** Probability distribution validation.

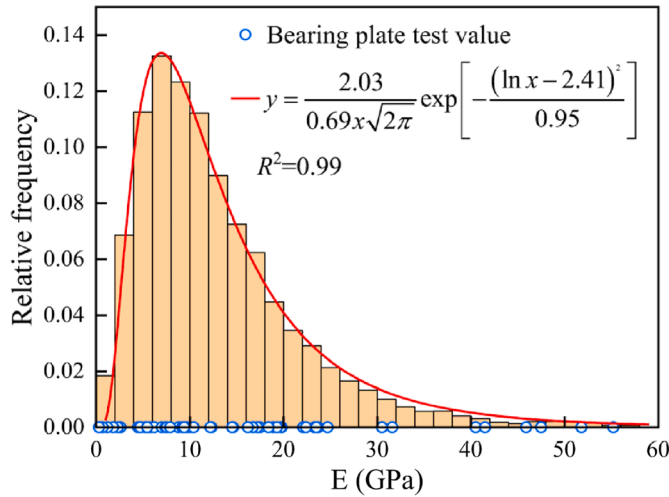


**Fig. 9.** Histogram of frequency distribution of deformation modulus.

comparison, the figure includes blue circles representing the parameter values obtained through the bearing plate test. A significant proportion of the simulated  $E$  samples, specifically 91%, fall within the interval [0 GPa, 25 GPa], while approximately 86% of the samples derived from the field test also fall within this interval. This agreement between the two distributions suggests that the simulated samples are more in line with reality.

A comparison of the deformation modulus results measured using the Bayesian method and the bearing plate test is presented in Table 7. The mean value of the bearing plate test results (a priori information) differs from the sample estimates (a posteriori information) by 1.1 GPa, while the difference in standard deviation amounts to 2.3 GPa. The standard deviation of the posterior distribution is smaller than that of the a priori distribution, indicating

that the data are more concentrated. This allows for random field parameterization to be performed based on the posterior probabilities.

To verify that the posterior probability distribution of the deformation modulus adheres to a lognormal distribution, the natural logarithm of the posterior sample values is first taken. Subsequently, the Q-Q plot is used to analyze the logarithmically transformed data (Fig. 10). In the Q-Q plot, the scatter points closely align with a straight line, indicating that the logarithm of the sample parameters follows a normal distribution. The relationship between the mean and standard deviation of  $E$  and the mean and standard deviation of  $\ln E$  is shown as follows:

$$\begin{aligned} \mu &= \exp\left(\mu_E + \sigma_E^2/2\right) \\ \sigma &= \exp\left(2\mu_E + \sigma_E^2\right) \left[ \exp\left(\sigma_E^2\right) - 1 \right] \end{aligned} \quad (15)$$

$\ln E$  follows a normal distribution with a mean of 2.41 and a standard deviation of 0.69. Table 8 presents the CRFs for the deformation modulus established using field bearing plate test data under different modes. The model employs the variance of the deformation modulus as the  $n$  value and calculates the natural logarithm of the bearing plate test data, which are utilized to determine the deformation modulus at specific locations to establish the CRF.

Al-Bittar and Soubra (2017) suggested that analysis error can be effectively reduced when the ratio of the grid size to correlation length is set at 0.2. For the CRF model, which measures 320 m  $\times$  320 m, as shown in Table 8, the grid size is configured at 5 m. This results in a total of 4096 grids, with each being represented by different color-coded parameter values. The spatial distribution pattern depicted in the model figures aligns closely with the distribution pattern of the random field in Table 5. The random field parameters obtained through this method are presented as natural logarithmic values, and the data in the figures have been converted into indices.

Several CRFs are generated using the parameters from mode b in Table 8. An interval of  $y = 140$  m (in which there were three

**Table 7**  
Summary of deformation modulus ( $E$ ) parameters.

Parameter	Bearing plate test (GPa)	Bayesian method (GPa)	Difference (GPa)
Mean	15.3	14.2	1.1
Standard deviation	13.4	11.1	2.3

**Table 8**  
CRF modeling of  $E$  in each mode.

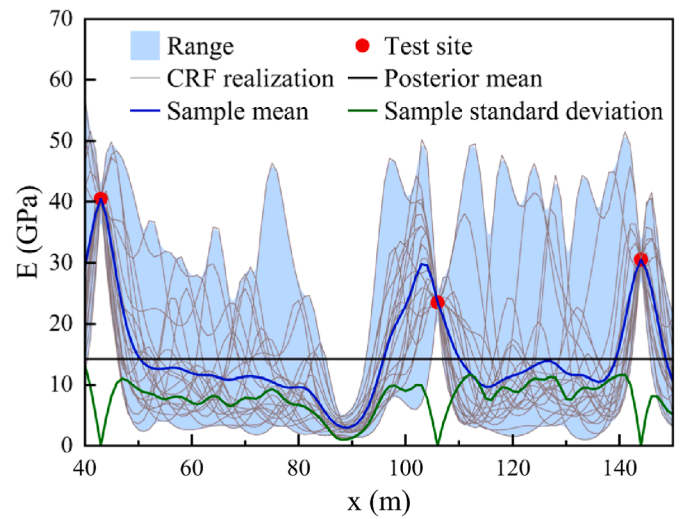
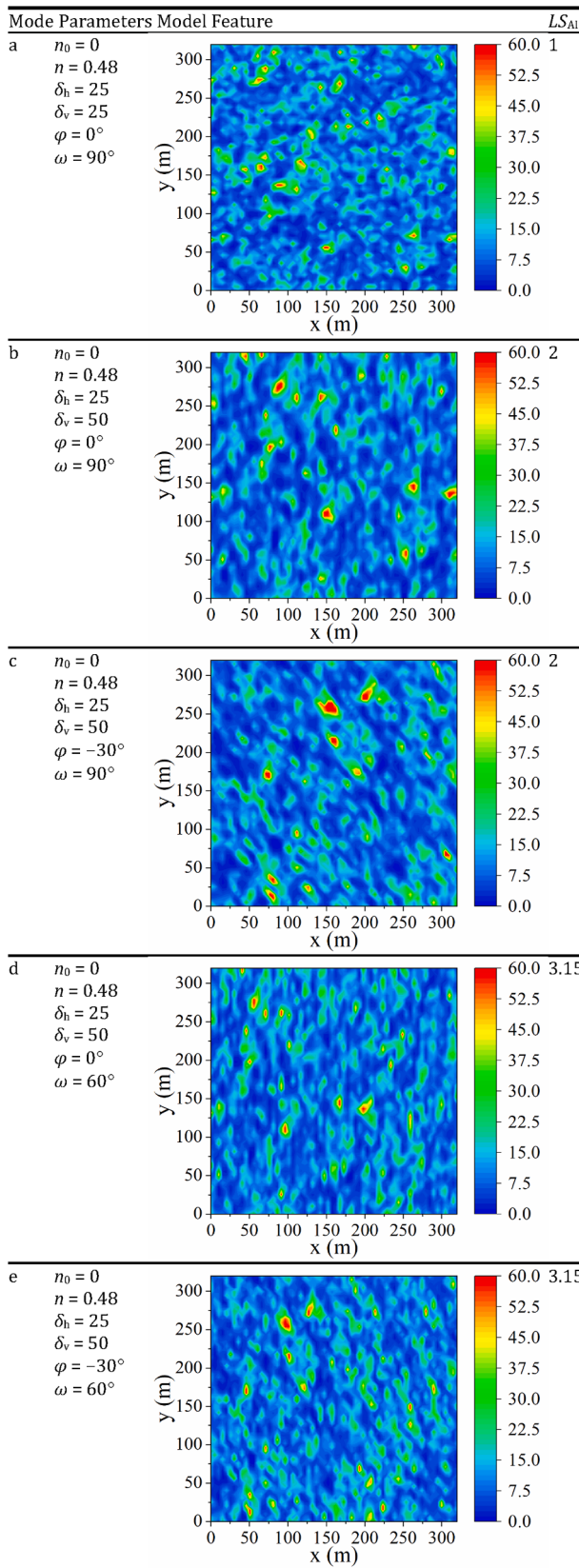


Fig. 11. Deformation modulus random field analysis.

bearing plate test sites) is selected for analysis, with  $x$  varying within the interval [40 m, 150 m] at 1 m intervals. Fig. 11 displays a set of 20 CRFs generated to calculate the means and standard deviations of the deformation modulus at different  $x$  distances. The mean values fluctuate around a straight line representing the posterior mean. The mean for the random field ensemble is 14.9 GPa, while the a posteriori mean is slightly lower at 14.2 GPa. As the distance from the field test point is reduced, the simulated parameters fluctuate, corresponding to a smaller standard deviation. The smaller standard deviation at  $x = 90$  m and  $y = 140$  m can be attributed to the proximity of a test point. These results indicate that the Kriging-based CRF simulation method is reasonable.

## 5. Discussion

As demonstrated in Table 8, a grid size of 5 m is defined. It is important to note that different grid sizes can significantly impact the simulated deformation modulus parameters. Fig. 12 illustrates a comparison of the average deformation modulus across different grid sizes, including 1 m, 2 m, 4 m, 5 m, 8 m, 10 m, and 16 m. For each grid size, 1000 simulations of the model were conducted, and the mean deformation modulus from each simulation was calculated. Subsequently, the mean value of the deformation modulus

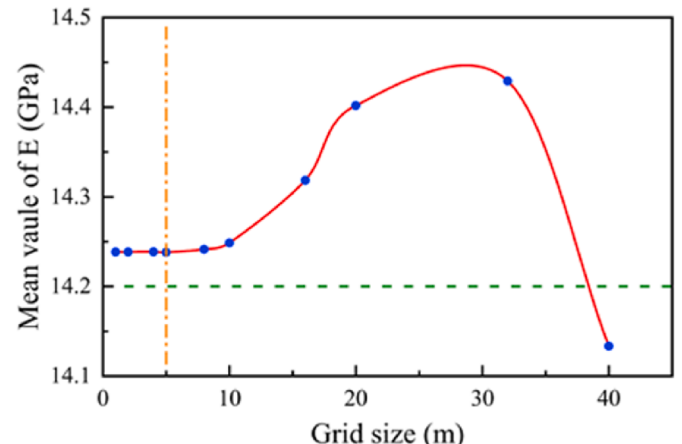


Fig. 12. Comparative diagram of grid size and mean value of  $E$ .

for each set of 1000 models was determined.

**Fig. 12** illustrates that when the grid size ranges from 1 m to 5 m, the mean value remains relatively stable and closely aligns with the a posteriori mean value. However, once the size exceeds 8 m, the fluctuation in the mean value becomes more pronounced. Though smaller grid sizes provide higher accuracy, they also lead to increased computation time. Therefore, a grid size of 5 m is identified as a suitable option.

This study presents a framework for constructing random fields and evaluating anisotropy. However, the proposed method has some limitations. Firstly, the proposed anisotropy metrics are designed for comparisons within the same mode, which limits the applicability for cross-mode anisotropy evaluation. Secondly, when employing Bayesian methods for the analysis, there are challenges related to model transformation uncertainty. The accuracy of the adopted single-parameter fitting is not particularly high. In future work, it is planned to adopt multi-parameter fitting to further improve the ability to deal with parameter uncertainty.

## 6. Conclusions

The present study presents a method for generating variability functions and random fields across different anisotropic modes by leveraging random field theory and the Kriging method. An anisotropy index is proposed to quantitatively assess the relationship between the autocorrelation length and the principal axis direction. The following conclusions are drawn:

- (1) Fracture pattern anisotropy based on fracture distribution is associated with the random field anisotropy considering the correlation scale.
- (2) A crucial metric is the random field anisotropy index ( $LS_{AI}$ ), which combines the principal axis direction and the autocorrelation length. An  $LS_{AI}$  value closer to 1 indicates a lower degree of anisotropy.
- (3) The more significant the autocorrelation length, the closer the connection between the parameters. The autocorrelation principal axis direction and rotation angle greatly influence the model construction.
- (4) A priori information about the deformation modulus is essential in shaping the posterior distribution of parameters. The results show that the distribution laws of the a posteriori and experimental parameters are largely consistent.

## CRediT authorship contribution statement

**Kejing Chen:** Visualization, Writing – original draft, Investigation, Software. **Qinghui Jiang:** Writing – review & editing, Conceptualization, Resources, Supervision.

## Declaration of competing interest

The authors declare that they have no known competing financial interests or personal relationships that could have appeared to influence the work reported in this paper.

## Acknowledgments

This research is financially supported by the Doctoral Research Funds for Nanchang HangKong University, China (Grant No. EA202411211). This support is gratefully acknowledged.

## References

- Al-Bittar, T., Soubra, A., 2017. Bearing capacity of spatially random rock masses obeying Hoek–Brown failure criterion. *Georisk* 11 (2), 215–229.
- Alemdag, S., Gurocak, Z., Cevik, A., Cabalar, A.F., Gokceoglu, C., 2016. Modeling deformation modulus of a stratified sedimentary rock mass using neural network, fuzzy inference and genetic programming. *Eng. Geol.* 203, 70–82.
- Bonneau, F., Caumon, G., Renard, P., 2016. Impact of a stochastic sequential initiation of fractures on the spatial correlations and connectivity of discrete fracture networks. *J. Geophys. Res. Solid Earth* 121 (8), 5641–5658.
- Bungenstab, F.C., Bicalho, K.V., 2016. Settlement predictions of footings on sands using probabilistic analysis. *J. Rock Mech. Geotech. Eng.* 8 (2), 198–203.
- Chen, K., Jiang, Q., 2023. Estimation of compliance tensor and anisotropy index for fractured rock masses using field measured data. *Eng. Geol.* 322, 107181.
- Chien, W., Lu, Y., Juang, C.H., Dong, J., Hung, W., 2022. Effect of stratigraphic model uncertainty at a given site on its liquefaction potential index: comparing two random field approaches. *Eng. Geol.* 309, 106838.
- Ching, J., Yoshida, I., Phoon, K., 2023. Comparison of trend models for geotechnical spatial variability: sparse Bayesian learning vs. Gaussian process regression. *Gondwana Res.* 123, 174–183.
- Chwala, M., Phoon, K., Uzelli, M., Zhang, J., Zhang, L., Ching, J., 2023. Time capsule for geotechnical risk and reliability. *Georisk* 17 (3), 439–466.
- Cui, J., Jiang, Q., Li, S., Feng, X., Zhang, M., Yang, B., 2017. Estimation of the number of specimens required for acquiring reliable rock mechanical parameters in laboratory uniaxial compression tests. *Eng. Geol.* 222, 186–200.
- Ering, P., Babu, G.L.S., 2016. Probabilistic back analysis of rainfall induced landslide – a case study of Malin landslide, India. *Eng. Geol.* 208, 154–164.
- Geyer, S., Papaioannou, I., Straub, D., 2021. Bayesian analysis of hierarchical random fields for material modeling. *Probab. Eng. Mech.* 66, 103167.
- Gravanis, E., Pantelidis, L., Griffiths, D.V., 2014. An analytical solution in probabilistic rock slope stability assessment based on random fields. *Int. J. Rock Mech. Min.* 71, 19–24.
- Guajardo, B., Pinto, F., Astroza, R., 2024. Effects of soil spatial variability on the seismic response of multi-span simply-supported highway bridges. *Bull. Earthq. Eng.* 22, 2643–2675.
- Guan, Z., Wang, Y., Phoon, K., 2024. Dictionary learning of spatial variability at a specific site using data from other sites. *J. Geotech. Geoenviron. Eng.* 150 (9), 04024072.
- Han, G., Zhang, C., Singh, H.K., Liu, R., Chen, G., Huang, S., Zhou, H., Zhang, Y., 2023. Characterizing large-scale weak interlayer shear zones using conditional random field theory. *J. Rock Mech. Geotech. Eng.* 15 (10), 2611–2625.
- Hua, D., Jiang, Q., Liu, R., Gao, Y., Yu, M., 2021. Rock mass deformation modulus estimation models based on in situ tests. *Rock Mech. Rock Eng.* 54 (11), 5683–5702.
- Jeffery, M., Huang, J., Fityus, S., Giacomini, A., Buzzi, O., 2021. A rigorous multiscale random field approach to generate large scale rough rock surfaces. *Int. J. Rock Mech. Min. Sci.* 142, 104716.
- Jiang, Q., Cui, J., Feng, X., Zhang, Y., Zhang, M., Zhong, S., Ran, S., 2017. Demonstration of spatial anisotropic deformation properties for jointed rock mass by an analytical deformation tensor. *Comput. Geotech.* 88, 111–128.
- Konkol, J., 2023. Incorporating installation effects into the probability analysis of controlled modulus columns. *Soils Found.* 63 (1), 101266.
- Krige, D.G., 1951. A statistical approach to some basic mine valuation problems on the Witwatersrand. *J. S. Afr. Inst. Min. Metall.* 52 (6), 119–139.
- Lasantha, H.S., Athapaththu, A.M.R.G., 2024. Advancing slope stability assessment in weathered metamorphic terrains: a probabilistic approach utilizing the SSPC method on Highland Complex, Sri Lanka. *Bull. Eng. Geol. Environ.* 83 (2), 54.
- Liu, J., Jiang, Q., Chen, T., Yan, S., Ying, J., Xiong, X., Zheng, H., 2022. Bayesian estimation for probability distribution of rock's elastic modulus based on compression wave velocity and deformation warning for large underground cavern. *Rock Mech. Rock Eng.* 55 (6), 3749–3767.
- Liu, W.F., Leung, Y.F., 2018. Spatial variability of saprolitic soil properties and relationship with joint set orientation of parent rock: insights from cases in Hong Kong. *Eng. Geol.* 246, 36–44.
- Maleki, A.T., Parviz, H., Khatibi, A.A., Zakeri, M., 2023. Probabilistic stability of uncertain composite plates and stochastic irregularity in their buckling mode shapes: a semi-analytical non-intrusive approach. *Front. Struct. Civ. Eng.* 17 (2), 179–190.
- Marrett, R., Gale, J.F.W., Gómez, L.A., Laubach, S.E., 2018. Correlation analysis of fracture arrangement in space. *J. Struct. Geol.* 108, 16–33.
- Mazraehli, M., Zare, S., 2020. An application of uncertainty analysis to rock mass properties characterization at porphyry copper mines. *Bull. Eng. Geol. Environ.* 79 (7), 3721–3739.
- Montoya-Noguera, S., Lopez-Caballero, F., 2023. Comparative study of homogenization techniques for evaluating the bearing capacity of bimaterials under shallow foundations. *Comput. Geotech.* 164, 105842.
- Pandey, A., Singh, A., Gardoni, P., 2022. A review of information field theory for Bayesian inference of random fields. *Struct. Saf.* 99, 102225.
- Pandit, B., Sivakumar Babu, G.L., 2021. Probabilistic stability assessment of tunnel-support system considering spatial variability in weak rock mass. *Comput. Geotech.* 137, 104242.
- Papaioannou, I., Straub, D., 2017. Learning soil parameters and updating geotechnical reliability estimates under spatial variability – theory and application to

- shallow foundations. *Georisk* 11 (1), 116–128.
- Rasel, H.M., Al Mamun, M.A., Hasnat, A., et al., 2023. Sustainable futures in agricultural heritage: geospatial exploration and predicting groundwater-level variations in Barind tract of Bangladesh. *Sci. Total Environ.* 865, 161297.
- Riquelme, A.J., Abellán, A., Tomás, R., 2015. Discontinuity spacing analysis in rock masses using 3D point clouds. *Eng. Geol.* 195, 185–195.
- Sasanian, S., Soroush, A., Jamshidi Chenari, R., 2020. Two-dimensional random field conditioned by CPT data: case study. *Int. J. Civ. Eng.* 18 (2), 123–136.
- Shen, X., Chen, M., Lu, W., Li, L., 2017. Using P wave modulus to estimate the mechanical parameters of rock mass. *Bull. Eng. Geol. Environ.* 76 (4), 1461–1470.
- Tian, Y., 2023. Anisotropy of surface morphology characteristics of rock discontinuity and its evaluation method. *Int. J. GeoMech.* 23 (12), 04023220.
- Vanmarcke, E., 2010. *Random Fields: Analysis and Synthesis*. World Scientific, Singapore.
- Wang, Y., Cao, Z., 2013. Probabilistic characterization of Young's modulus of soil using equivalent samples. *Eng. Geol.* 159, 106–118.
- Wang, Y., Zhao, T., Phoon, K., 2018. Direct simulation of random field samples from sparsely measured geotechnical data with consideration of uncertainty in interpretation. *Can. Geotech. J.* 55 (6), 862–880.
- You, M., Zuo, C., Tan, F., Lv, J., 2024. Effect of heterogeneity of particle properties on the mechanical properties of sandy soil materials. *Comput. Geotech.* 165, 105890.
- Zhang, W., Han, L., Gu, X., Wang, L., Chen, F., Liu, H., 2022. Tunneling and deep excavations in spatially variable soil and rock masses: a short review. *Undergr. Space* 7 (3), 380–407.
- Zhang, Z., Zhang, Y., Zhang, L., Cao, Z., Wang, Y., Yu, Y., Zheng, J., 2025. Characterizing the spatial variability of marine soil properties with site-specific sparse data using a Bayesian data fusion approach. *Acta Geotech.* 20, 765–779.
- Zhu, H., Zhang, L.M., 2013. Characterizing geotechnical anisotropic spatial variations using random field theory. *Can. Geotech. J.* 50 (7), 723–734.



**Qinghui Jiang** obtained his PhD degree from the Institute of Rock and Soil Mechanics, Chinese Academy of Sciences in 2000. He is now a professor and doctoral supervisor at the School of Civil Engineering at Wuhan University, China. His research interests include (1) stability analysis of high rock slopes; (2) numerical calculation of large-scale rock engineering; (3) geometric characteristics and digital model of rock mass structures; and (4) special concrete and rock reinforcement support structures. He has presided over five National Natural Science Foundation of China and numerous significant engineering projects, and has published over 100 scientific papers, 30 authorized invention patents, and ten software publications.